www.lajss.org
Latin American Journal of Solids and Structures 1 (2003) 141–166

An adaptive continuum/discrete crack approach for meshfree particle methods

T. Rabczuk and T. Belytschko*

Department of Mechanical Engineering, Northwestern University, 2145 Sheridan Road, Evanston, IL 60208-311, U.S.A.

Abstract

A coupled continuum/discrete crack model for strain softening materials is implemented in a meshfree particle code. A coupled damage plasticity constitutive law is applied until a certain strain based threshold value - this is at the maximum tensile stress of the equivalent uniaxial stress strain curve - is reached. At this point a discrete crack is introduced and described as an internal boundary with a traction crack opening relation. Within the framework of meshfree particle methods it is possible to model the transition from the continuum to the discrete crack since boundaries and particles can easily be added and removed. The EFG method and an explicit time integration scheme is used. The integrals are evaluated by nodal integration, an integration with stress points and also a full Gauss quadrature. Some results are compared to experimental data and show good agreement. Additional comparisons are made to a pure continuum constitutive law.

Keywords: meshfree methods, discrete crack model, concrete, loss of hyperbolicity

1 Introduction

When modelling materials with strain softening, pure continuum based constitutive laws have difficulties because the loss of hyperbolicity of the PDE results in localization to a set of measure zero in rate independent materials, see Bazant and Belytschko [4]. The resulting spurious mesh dependency requires regularization techniques. Within the framework of meshfree methods, it is easily possible to treat discrete discontinuities, so that it is not necessary to describe the softening regime within the constitutive model. Hence, the difficulty mentioned above can be avoided.

A softening regime is observed in the macroscopic stress strain curve, i.e. the stresses decrease with increasing strain, when a material undergoes sufficient damage. Detailed studies (see e.g. [18, 21]) in brittle materials such as concrete and ceramics have shown that microcracks are initiated and later form macrocracks. The formation of a visible macrocrack is generally assumed to occur when the stress strain curve reaches its maximum tensile stress. Because of

* Corresponding author Email: tedbelytschko@northwestern.edu Received 19 Sep 2003; Revised 30 Oct 2003

the roughness of the crack edges, traction forces still can be transmitted along the crack close to the crack tip until the material separates completely.

In continuum based material models, plasticity and/or damage models are applied to reproduce this constitutive behavior. However, difficulties occur with the onset of softening since the PDE changes its type. In static problems this leads to the loss of elipticty, in dynamic problems to the loss of hyperbolicity. Several regularization techniques have been developed to avoid this shortcoming. In the case of damage models, a viscous damage can be added, so that the hyperbolicity is retained as shown in [27]. Viscoplastic models also avoid the loss of hyperbolicity and mesh dependency, see e.g. Belytschko et al. [11], Needleman [22], Loret et al. [3]. A more natural way is to treat the macrocrack as a discontinuity. Meshfree particle methods are well suited for such approaches since boundaries and particles can be added adaptively quite easily. In this paper we will propose a continuum/discrete crack approach within the framework of meshfree particle methods based on an adaptive refinement scheme.

The article is arranged as follows. First, the EFG method is briefly reviewed. Then the weak form of the linear momentum equation will be derived for treating the discontinuity, i.e. the crack, as an internal boundary. The discrete crack is modelled via the visibility criterion. Its mechanics is described by a traction crack opening model for concrete materials. In section 3 the combined continuum/discrete crack approaches will be proposed. Implementation details are discussed. Finally, the approaches are tested and applied to notched concrete beams under quasistatic and dynamic loading. The beams fail because of a mixed mode (mode I-II) fracture. Crack patterns and load displacement curves for several beams with different locations of the notch are compared to experimental data and show good agreement.

2 A discrete crack approach in the element free Galerkin method

2.1 Meshfree approximation

The meshfree MLS-approximation in a Lagrangian description can be written as

$$u(\mathbf{X}, t) = \mathbf{p}^T(\mathbf{X})\ \mathbf{a}(\mathbf{X}, t) \tag{1}$$

where $\mathbf{X}$ are the material coordinates, t is the time and a $\mathbf{p}$ are linear basis functions $\mathbf{p}(\mathbf{X}) = (1\ X\ Y)\ \forall \mathbf{X} \in \Re^2$. Minimizing

$$J = \sum_{I \in S} \left(\mathbf{p}_I^T(\mathbf{X})\ \mathbf{a}(\mathbf{X}, t) - u_I(t)\right)^2\ W(\mathbf{X} - \mathbf{X}_I, h) \tag{2}$$

with respect to $\mathbf{a}$ leads to the approximation

$$u(\mathbf{X}, t) = \sum_{I \in S} \Phi_I(\mathbf{X})\ u_I(t) \tag{3}$$

where $\Phi_I(\mathbf{X})$ is the shape function of particle I, S is the set of neighbor particles for $\mathbf{X}$, u_I is the value at the particle at the position $\mathbf{X}_I$, $W(\mathbf{X}-\mathbf{X}_J,h)$ is a window function and h is the interpolation radius of the window function. In the EFG-method (see Belytschko et al. [9, 10]) the shape functions are:

$$\Phi_J = \mathbf{p}^T(\mathbf{X}) \cdot \mathbf{A}(\mathbf{X})^{-1} \cdot \mathbf{B}(\mathbf{X}) \tag{4}$$

$$\mathbf{A}(\mathbf{X}) = \sum_{J \in S} \mathbf{p}_J(\mathbf{X})\ \mathbf{p}_J^T(\mathbf{X})\, W(\mathbf{X}-\mathbf{X}_J,h) \tag{5}$$

$$\mathbf{B}(\mathbf{X}) = \sum_{J \in S} \mathbf{p}_J(\mathbf{X})\, W(\mathbf{X}-\mathbf{X}_J,h) \tag{6}$$

Lagrangian kernels, i.e. kernels that are functions of material coordinates, are used in the above because of their improved stability properties, see Belytschko et al. [7, 25].

2.2 The discrete linear momentum equation

Consider a body Ω whose undeformed image is Ω_0 with boundary Γ_0. The strong form of the linear momentum equation is:

$$\nabla \cdot \boldsymbol{P} + \varrho_0\ \mathbf{b} = \varrho_0\ \ddot{\mathbf{u}}\ \ in\ \ \Omega_0 \tag{7}$$

and the boundary conditions are

$$\mathbf{n}_0 \cdot \mathbf{P} = \bar{\mathbf{t}}_0\ \ in\ \ \Gamma_0^t \tag{8}$$

$$\mathbf{u} = \bar{\mathbf{u}}\ \ in\ \ \Gamma_0^u \tag{9}$$

where $\mathbf{P}$ is the nominal stress, ϱ_0 is the initial density, $\mathbf{b}$ are the body forces, $\mathbf{u}$ and $\ddot{\mathbf{u}}$ are the displacements and accelerations, respectively, $\mathbf{n}_0$ is the normal to the boundary in the initial configuration and $\bar{\mathbf{u}}$ and $\bar{\mathbf{t}}$ denote the applied displacements and tractions, respectively; $\Gamma_0^u \bigcup \Gamma_0^t = \Gamma_0$; $\Gamma_0^u \bigcap \Gamma_0^t = 0$. The weak form of the linear momentum equation is obtained by multiplying the momentum equation with the test functions $\delta\mathbf{u}$ and integrating over the domain:

$$\int_{\Omega_0} \nabla \cdot \mathbf{P} \cdot \delta\mathbf{u}\ d\Omega_0 + \int_{\Omega_0} \varrho_0\,(\mathbf{b}-\ddot{\mathbf{u}}) \cdot \delta\mathbf{u}\ d\Omega_0 = 0 \tag{10}$$

The first term on the RHS of the momentum equation can be transformed by integration by parts

$$\int_{\Omega_0} \nabla \cdot \mathbf{P} \cdot \delta\mathbf{u}\ d\Omega_0 = \int_{\Omega_0} \nabla \cdot (\mathbf{P} \cdot \delta\mathbf{u})\ \ d\Omega_0 - \int_{\Omega_0} (\nabla \otimes \delta\mathbf{u})^T : \mathbf{P}\ d\Omega_0 \tag{11}$$

Using the Gauss theorem, the first term on the RHS of equation (11) can be written as

$$\int_{\Omega_0} \nabla \cdot (\mathbf{P} \cdot \delta\mathbf{u})\ \ d\Omega_0 = \int_{\Gamma_0^t} \mathbf{n}_0 \cdot \mathbf{P} \cdot \delta\mathbf{u}\ d\Gamma_0 + \int_{\Gamma_0^{cA}} \mathbf{n}_0^A \cdot \mathbf{P}^A \cdot \delta\mathbf{u}^A\ d\Gamma_0 + \int_{\Gamma_0^{cB}} \mathbf{n}_0^B \cdot \mathbf{P}^B \cdot \delta\mathbf{u}^B\ d\Gamma_0 \tag{12}$$

where the second and third term on the right hand side represent the traction at the crack boundary as illustrated in figure 1. The crack can be considered as an internal boundary with two crack edges as shown in figure 1 with $\mathbf{\Gamma}_0^c = \mathbf{\Gamma}_0^{cA} \bigcup \mathbf{\Gamma}_0^{cB}$.

With the relation $\mathbf{t}_0^A = \mathbf{n}_0^A \cdot \mathbf{P}^A$, $\mathbf{t}_0^B = \mathbf{n}_0^B \cdot \mathbf{P}^B$ and under the assumption that $\mathbf{n}_0^A = -\mathbf{n}_0^B$, the weak Galerkin form of the linear momentum equation including a discontinuity is then:

$$\int_{\Omega_0} \varrho_0\ \delta\mathbf{u} \cdot \ddot{\mathbf{u}}\ d\Omega_0 + \int_{\Omega_0} (\nabla \otimes \delta\mathbf{u})^T : \mathbf{P}\ d\Omega_0 - \int_{\Omega_0} \varrho_0\ \delta\mathbf{u} \cdot \mathbf{b}\ d\Omega_0 \\ - \int_{\Gamma_0^t} \delta\mathbf{u} \cdot \bar{\mathbf{t}}_0\ d\Gamma - \int_{\Gamma_0^{cA}} \mathbf{t}_0^A \cdot \delta\mathbf{u}^A\ d\Gamma_0 - \int_{\Gamma_0^{cB}} \mathbf{t}_0^B \cdot \delta\mathbf{u}^B\ d\Gamma_0 = 0 \tag{13}$$

Assuming that the traction $\mathbf{t}_0^A = -\mathbf{t}_0^B$, the weak form of the linear momentum equation can be written as

$$\int_{\Omega_0} \varrho_0\ \delta\mathbf{u} \cdot \ddot{\mathbf{u}}\ d\Omega_0 + \int_{\Omega_0} (\nabla \otimes \delta\mathbf{u})^T : \mathbf{P}\ d\Omega_0 - \int_{\Omega_0} \varrho_0\ \delta\mathbf{u} \cdot \mathbf{b}\ d\Omega_0 \\ - \int_{\Gamma_0^t} \delta\mathbf{u} \cdot \bar{\mathbf{t}}_0\ d\Gamma - \int_{\Gamma_0^c} \mathbf{t}_0 \cdot [\![\delta\mathbf{u}]\!]\ d\Gamma_0 = 0 \tag{14}$$

where $\delta\mathbf{u} \in V_0$ are the test functions and $\mathbf{u} \in V_1$ are the trial functions. The same test and trial functions are used for $\delta\mathbf{u}$ and $\mathbf{u}$. The spaces V_0 and V_1 are as follows:

$$V_1 = \left(\mathbf{u}|\mathbf{u}\ \in\ H^1(\Omega),\ \mathbf{u}\ \textit{discontinuous on}\ \Gamma_0^c\ \mathbf{u} = \bar{\mathbf{u}} \quad on \quad \Gamma_u\right) \tag{15}$$

$$V_0 = V_1 \bigcap (\delta\mathbf{u}|\delta\mathbf{u} = 0 \quad on \quad \Gamma_u) \tag{16}$$

The test and the trial functions are approximated via the following equations:

$$\delta\mathbf{u}^h(\mathbf{X}) = \sum_J \Phi_J(\mathbf{X})\ \delta\mathbf{u}_J \tag{17}$$

$$\mathbf{u}^h(\mathbf{X}, t) = \sum_J \Psi_J(\mathbf{X})\ \mathbf{u}_J(t) \tag{18}$$

Substituting (17) and (18) into (14) gives

$$\sum_I \int_{\Omega_0} \varrho_0\ \Phi_J(\mathbf{X})\ \Phi_I(\mathbf{X})\ d\Omega_0\ \ddot{\mathbf{u}}_I = \int_{\Omega_0} \varrho_0\ \Phi_I\ \mathbf{b}\ d\Omega_0 + \\ \int_{\Gamma_0^t} \Phi_I\ \bar{\mathbf{t}}_0\ d\Gamma_0 + \int_{\Gamma_0^c} [\![\Phi_I]\!]\ \bar{\mathbf{t}}_0\ d\Gamma_0 - \int_{\Omega_0} \nabla\Phi_I \cdot \mathbf{P}\ d\Omega_0 \tag{19}$$

The integrals are evaluated numerically by nodal integration, a combination of nodal integration with stress points or a full Gauss quadrature based on a background mesh, see Rabczuk et al. [25]. A detailed description how to integrate over the crack domain is given in the following sections.

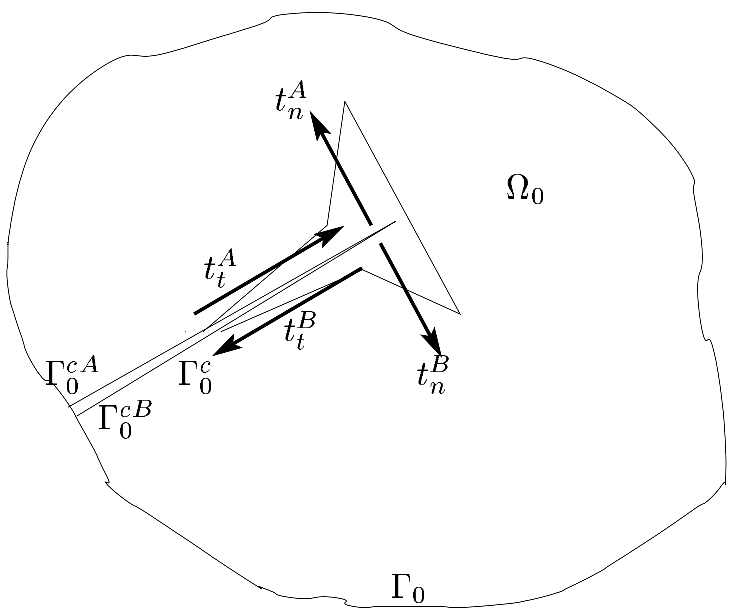

Figure 1: Domain with crack boundary

2.3 The discrete crack model

According to figure 1 the crack surface integral is:

$$\int_{\Gamma_0^c} \mathbf{t}_0 \cdot [\![\delta \mathbf{u}]\!] \; d\Gamma_0 = \int_{\Gamma_0^c} \left(\mathbf{t}_0^A \cdot \delta \mathbf{u}^A + \mathbf{t}_0^B \cdot \delta \mathbf{u}^B \right) \; d\Gamma_0 \tag{20}$$

The traction $\mathbf{t}_0$ along the boundary Γ_0^c depends on the jump in the displacement $[\![\mathbf{u}]\!]$. Let $\mathbf{t}_0^A$ be the traction on Γ_0^{cA} and $\mathbf{t}_0^B$ the traction on boundary Γ_0^{cB} as shown in figure 1; note that $\mathbf{t}_0^A = -\mathbf{t}_0^B$. The tractions $\mathbf{t}_0^A$ and $\mathbf{t}_0^B$ can be expressed as a function of the jump in the displacement:

$$\mathbf{t}_0^A = \boldsymbol{\tau}_0^A([\![\mathbf{u}]\!]) = \boldsymbol{\tau}_0^A(\mathbf{u}^A - \mathbf{u}^B) = -\mathbf{t}_0^B \tag{21}$$

where $[\![\mathbf{u}]\!]$ represents the relative displacements between the crack surfaces Γ_0^{cA} and Γ_0^{cB}, i.e. the crack opening and is given by

$$[\![\mathbf{u}]\!] = \mathbf{u}(\mathbf{X}^A) - \mathbf{u}(\mathbf{X}^B) = \sum_I \Phi_I(\mathbf{X}^A) \; \mathbf{u}_I - \sum_I \Phi_I(\mathbf{X}^B) \; \mathbf{u}_I \tag{22}$$

2.3.1 Treatment of the discontinuity via the visibility criterion

The discontinuity, i.e. the jump in the displacement, is modelled via the visibility criterion. Therefore, any node J is excluded from $S_{\mathbf{X}_I}$ if the line $\bar{\mathbf{X}_I \mathbf{X}_J}$ intersects the discontinuity (see

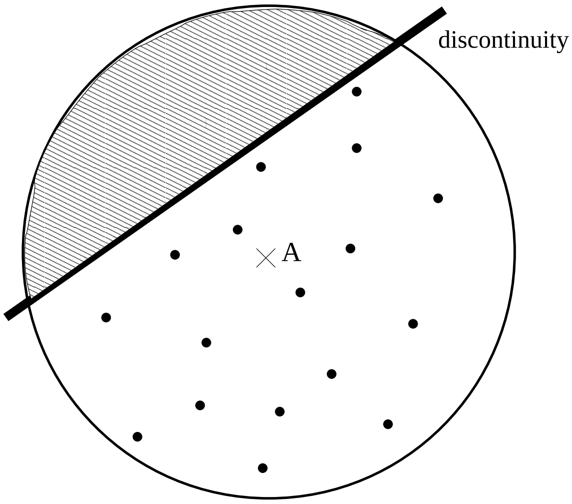

Figure 2: The visibility criterion; shaded area shows the nodes that have no influence on the approximation at point A

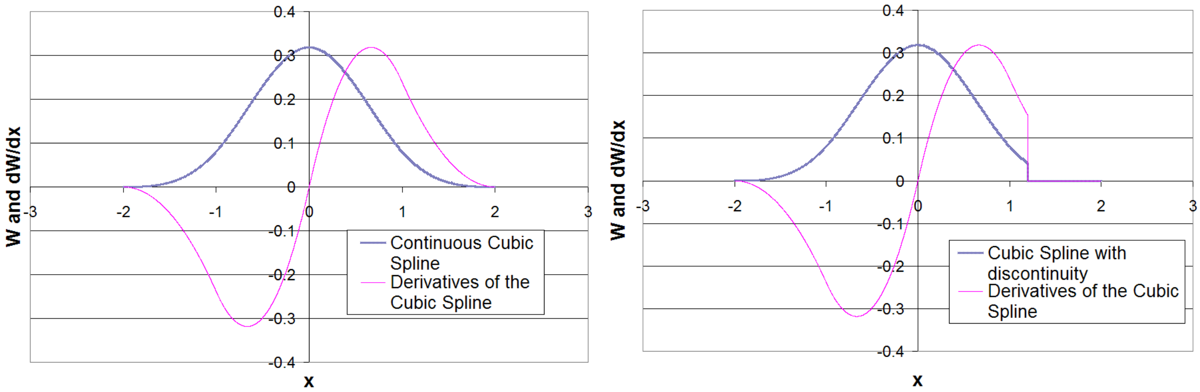

Figure 3: The one dimensional cubic spline and its derivative, left: without discontinuity, right: with discontinuity at x=1.2

figure 3 and 2). The LHS of figure 3 shows the continuous one dimensional cubic spline. On the RHS we assume a discontinuity at $x = 1.2$, where the cubic spline is cut.

We will briefly describe how to implement the visibility criterion in 2D. Consider the vectors $\mathbf{g}$ from $\mathbf{b}$ to $\mathbf{e}$, $\bar{\mathbf{g}}$ from $\mathbf{x}$ to $\mathbf{b}$ and $\hat{\mathbf{g}}$ from $\mathbf{x}$ to $\hat{\mathbf{x}}$ as illustrated in figure 4. For the vectors $\tilde{\lambda}\mathbf{g}$, $\bar{\mathbf{g}}$ and $\hat{\lambda}\hat{\mathbf{g}}$, we can write (23):

$$\bar{\mathbf{g}} + \tilde{\lambda}\,\mathbf{g} = \hat{\lambda}\,\hat{\mathbf{g}} \tag{23}$$

which can also be written as

$$\mathbf{G}\,\boldsymbol{\lambda} = \bar{\mathbf{g}} \tag{24}$$

with

$$\mathrm{G} = \begin{bmatrix} -g_x & \hat{g}_x \\ -g_y & \hat{g}_y \end{bmatrix} \qquad \boldsymbol{\lambda} = \begin{bmatrix} \tilde{\lambda} \\ \hat{\lambda} \end{bmatrix} \qquad \bar{\mathbf{g}} = \begin{bmatrix} \bar{g}_x \\ \bar{g}_y \end{bmatrix}$$

The straight lines $\mathbf{g}$ and $\hat{\mathbf{g}}$ have a common intersection $\mathbf{s}$, if $0 < \tilde{\lambda} < 1$ and $0 < \hat{\lambda} < 1$. If $det\ \mathbf{G} = 0$, the vectors $\mathbf{g}$ and $\hat{\mathbf{g}}$ are parallel. For convex discontinuities, the visibility criterion seems to be suitable. For non convex discontinuities such as kinks and crack edges (end-points in 2D), Belytschko et al. [6] and Organ et al. [23] proposed other methods such as the diffraction or transparency method. Since we don't expect nonconvex discontinuities in our applications, only the visibility criterion is applied, but the approach can easily be extended to the other two ones as described in [6] and [23].

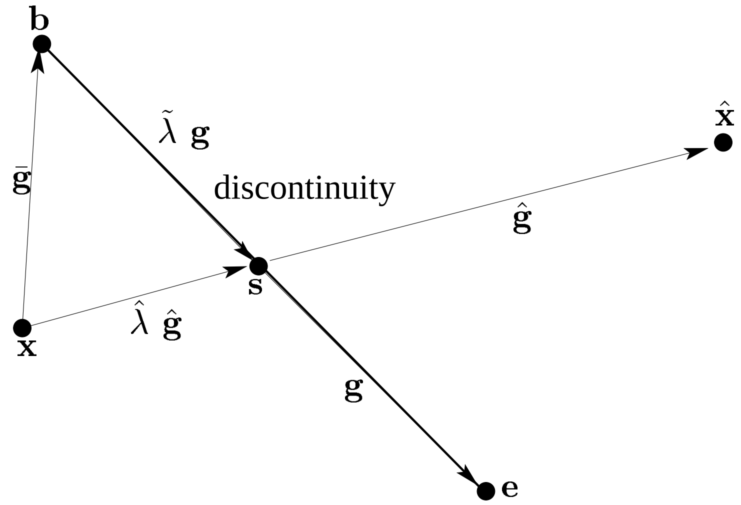

Figure 4: A crack modelled with the visibility criterion

2.3.2 The traction crack opening model

A traction crack opening model according to the EC2-model [1] is chosen. The traction depends on the crack opening w normal to the crack and the relative displacement u tangential to the crack, see figure 1. The normal traction is given by:

$$\mathrm{t}_n = \begin{cases} f_{ctm}(1-0.85w/w_1) & 0 \leq w < w_1 \\ 0.15\ f_{ctm}\frac{w_c-w}{w_c-w_1} & w_1 \leq w \leq w_c \\ 0 & w > w_c \end{cases} \tag{25}$$

with $w_1 = 2G_f/f_{ctm} - 0.15w_c$ and $w_c = \alpha_f\ G_f/f_{ctm}$, where α_f depends on the type of concrete and can be found in the EC2 [1] and f_{ctm} is the average of the uniaxial tensile strength of concrete according to the EC2 [1]. The fracture energy G_f is defined as

$$G_f = \int_0^{w_c} t_n(w)\ dw \tag{26}$$

and is a material parameter corresponding to the type of concrete, see [1]. For the tangential displacement a simple Coulomb friction model is used:

$$\mathrm{t}_\tau = \begin{cases} \beta f_n u/u_a & u \leq u_a \\ \beta f_n & u > u_a \end{cases} \tag{27}$$

where we have chosen $u_a = 2/3\ w_c$ and $\beta = 0.5$ since good agreement with some experimental data was obtained. In the next section the coupled continuum discrete crack model will be described in detail. A coupled damage plasticity constitutive law as described in Rabczuk and Eibl [26] is used for the concrete before the transition to the discrete crack model.

3 Continuum/discrete crack model

The continuum discrete crack model is applied to concrete and is implemented in a meshfree particle code. The integrals can be evaluated by different techniques (nodal integration, integration with stress points and Gauss quadrature based on a background mesh, see Rabczuk et al. [25]). Although the general procedure is independent of the integration technique, full Gauss quadrature creates some difficulties, e.g. the stable time step is reduced if the crack divides the integration cell into very small subcells (see figure 9). Moreover, full Gauss quadrature is more expensive and in this particular problem more difficult to implement. In our study we consider only the propagation of cracks from a given crack, but we will also present an approach to initiate a crack.

3.1 Criteria for crack propagation and initiation

As mentioned earlier, the main idea of this method is to switch from a continuum based constitutive law (stress strain law) to a discrete crack model (traction crack opening model) when required by the constitutive law, see figure 6. For the continuum model, a constitutive model described in [26] is adopted. A crack is initiated or propagated at particles where the PDE loses hyperbolicity. Especially in two or three dimensions, the transition point cannot easily be determined.

Several approaches such as the hoop stress criterion or the loss of hyperbolicity criterion were developed, see Belytschko et al. [5]. A sufficient condition of a hyperbolic PDE is a positive definite tangent modulus of the stress-strain relation. If the acoustic tensor $\mathbf{Q} = \mathbf{n}_0 \cdot \mathbf{C} \cdot \mathbf{n}_0$ is positive definite, hyperbolicity of the PDE is guaranteed. Belytschko et al. [5] obtained from the loss of hyperbolicity criterion also the direction and the length of the crack, i.e. crack speed. The hyperbolicity criterion requires that

$$e = min_{\mathbf{n}_0\ \mathbf{h}_0} (\mathbf{n}_0 \otimes \mathbf{h}_0 : \mathbf{C} : \mathbf{n}_0 \otimes \mathbf{h}_0) \geq 0 \tag{28}$$

where $\mathbf{C}$ is the tangent modulus of the stress-strain curve and $\mathbf{n}_0$ and $\mathbf{h}_0$ are two arbitrary unit vectors. The unit vector $\mathbf{n}_0$ and $\mathbf{h}_0$ are determined by a minimization procedure. The crack is propagated perpendicular to the unit vectors $\mathbf{n}_0$. Sometimes problems may occur, e.g. when the crack branches, since there may exist more than one solution in the minimization procedure. Other criteria can be used, e.g. $e = \bar{\sigma} - f_t$ where $\bar{\sigma}$ is the equivalent stress of the stress tensor and f_t is the tensile stress.

We have chosen a simpler approach for crack initiation and propagation as well as the direction and length of the crack. There is a major difference between the approach here and the approach in [13]. While in [13], the crack is propagated arbitrary through an element, hence no remeshing is necessary, we have to refine around the crack.

The transition from the continuum model to the discrete crack model takes place after exceeding a given strain value of the equivalent uniaxial stress strain curve as shown in figure 6. According to experimental data, this is the case when the equivalent uniaxial stress strain curve reaches its maximum tensile stress. At the beginning of the traction crack opening relation, the relative displacements between the crack edges are zero. At this time, the traction has a maximum $\mathbf{t}_0^{max} = \mathbf{n} \cdot \mathbf{P}^{max}$ and is decreasing to zero during the course of the load history. Actually, this is not remarkable, but it is mentioned because it is a major difference to other models (see e.g. Haeusler [16]), which don't treat the crack as an internal boundary and where $\mathbf{t}_0^{max} \neq \mathbf{n}_0 \cdot \mathbf{P}^{max}$ since the relative displacements are nonzero at the beginning of the discrete crack approach.

As just mentioned, a crack is initiated or propagated if a strain threshold is exceeded. First, imagine a given crack as shown in figure 5. Suppose the strain threshold is exceeded for particle B close to the crack tip. The crack will propagate in the direction of this particle. We treat the crack by two adjacent surfaces as illustrated in figure 6. Hence, particle B is split into two new particles. The particle split requires the recomputation of the new particle masses. They might be computed according to a Voronoi diagram where the new crack boundary has to be taken into account, see figure (7). More simply, the masses can be halved when a particle is split. Since an adaptive refinement is used to obtain good resolution near the crack, the masses of all affected particles have to be recomputed. Therefore, we compute the consistent mass matrix

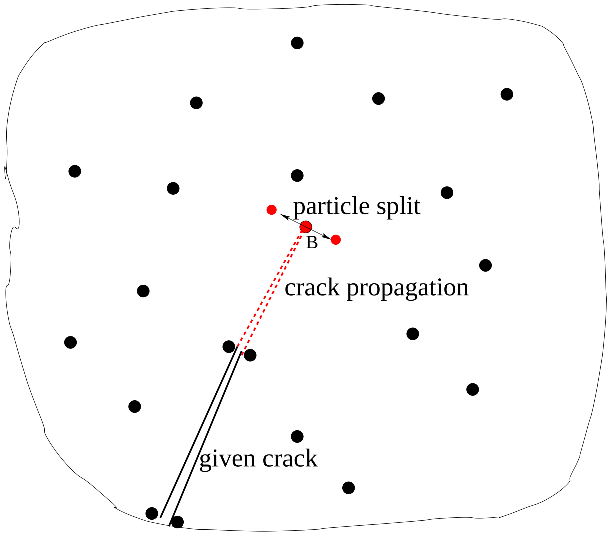

Figure 5: Scheme of crack propagation and particle split

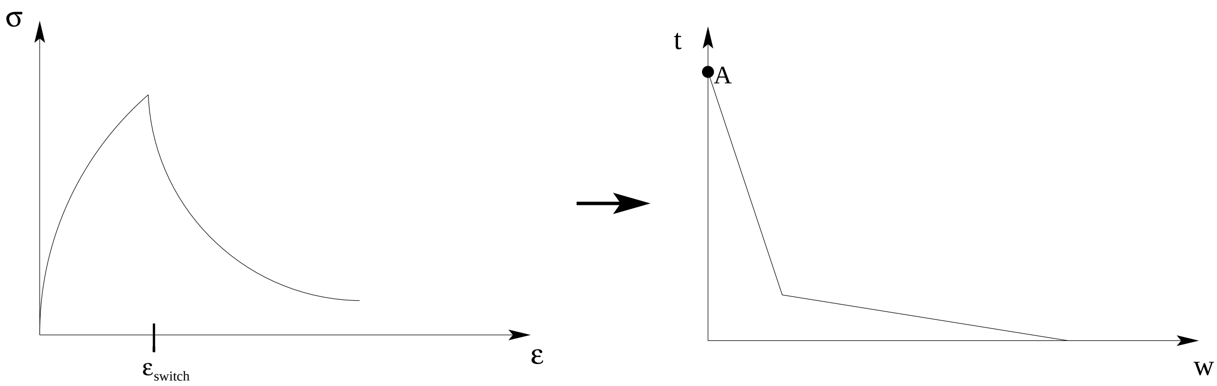

Figure 6: Switch from the continuum model to discrete crack model

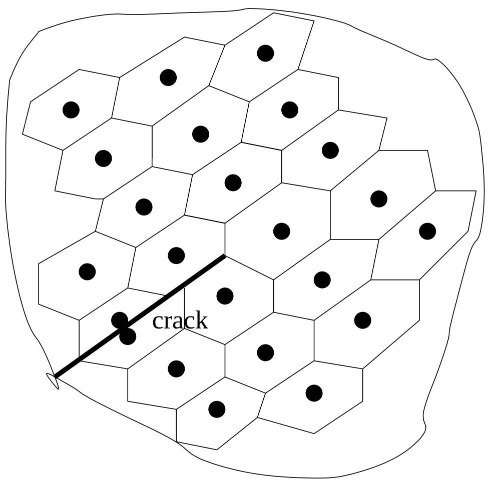

Figure 7: Voronoi cells for a particle arrangement with a crack

after every adaptation step. The diagonal mass matrix is obtained by a row sum technique as described in Belytschko et al. [8]. All other data are kept from the original particle.

The strain based criteria can also be used for crack initiation. For a mode I crack, the crack is initiated perpendicular to the direction of the principal tensile stress for the corresponding particle. Besides of the direction, a crack length has to be chosen. For simplicity, we have kept the crack length constant for a given time step but other approaches are possible, too. A crack length of $\alpha\ \delta x$, where $\delta x = \sqrt{dx^2 + dy^2}$ and $0 < \alpha < 1$, seems to be reasonable. The distance between two adjacent particles in the x-direction and y-direction is hereby denoted as dx and dy, respectively.

It has to be mentioned, that several problems occur if the integrals are evaluated by Gauss quadrature. One disadvantage is that the stable time step is significantly reduced if the crack divides a background cell into a very small cell as shown in figure 9. Implicit-explicit time integration has to be used, see Belytschko et al. [12] or Hughes et al. [19]. The second point is the high computational cost of full quadrature. Hence, we have chosen stress point integration so that we benefit from the truly meshfree character. An approach for a crack propagation using Gauss quadrature is proposed by Haeusler et al. [16] and will be used for comparison.

3.2 Determination of the crack direction and length

To obtain good resolution near the crack and to insure that the crack is propagated in the correct direction, high particle resolution near the crack, particularly the crack tip, is necessary. Therefore, an adaptive refinement is used at locations with high strain gradients, that is along the crack. The adaptive approach is explained in detail in Rabczuk et al. [24] and the description will be omitted here. The particles are added in a rectangular pattern. However, adaptation

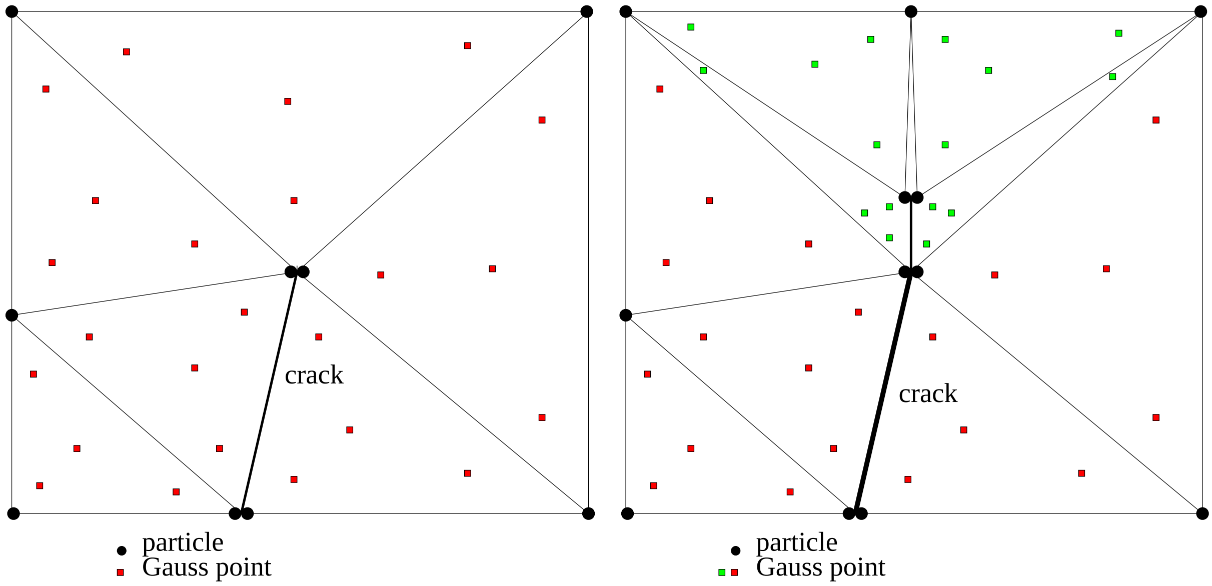

Figure 8: Crack propagation scheme and triangulation using an integration scheme based on a background mesh

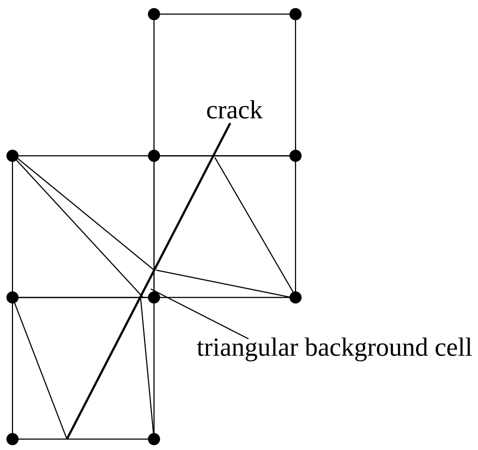

Figure 9: Stable time step for an element cut by a crack

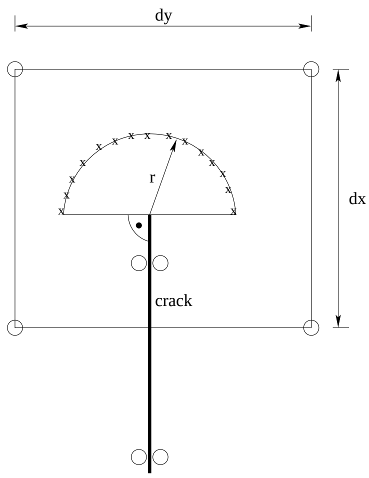

Figure 10: Scheme for the circular refinement

in only a rectangular pattern entails some drawbacks since the crack is then constrained by the rectangular pattern and a zigzag pattern in the path of the crack can sometimes be observed, see figure 17. If only straight cracks are considered, adequate results can be obtained when using a high particle resolution around the crack.

To obtain better crack paths, an additional technique similar to the one of Hao et al. [17] is applied. In addition to the 'usual' adaptive refinement, particles are added adaptively in a half circle around the crack tip as illustrated in figure 10. They are distinguished from the other particles by a superimposed x. All data is interpolated from the neighbor particles which are denoted by a superimposed o. The stresses and strains for such particles are:

$$\mathbf{F}^x = \sum_J \nabla\Phi(\mathbf{X}^x - \mathbf{X}^o_J, h)\ \mathbf{u}^o_J\ \ , \mathbf{P}^{x,t+dt} = \mathbf{P}^{x,t} + \mathbf{E}^x_t : \mathbf{F}^x \tag{29}$$

The stresses $\mathbf{P}^{x,t}$ are interpolated from the original particles. The stresses $\mathbf{P}^{x,t+dt}$ can be obtained directly from the total deformation tensor $\mathbf{F}$ or by interpolation.

A crucial point is the choice of the radius r of the half circle. It is chosen as the minimum particle distance $\delta x = \sqrt{dx^2 + dy^2}$ to $r = \alpha\ min\ \delta x$, with $0.25 < \alpha < 1$. Some results using this technique are shown in section 4. Figure 17c and figure 17d show two results obtained with this approach and for two values of α ($\alpha = 0.95$ and $\alpha = 0.5$) compared to the 'usual' adaptive refinement. For these examples, 37 and 73 additional particles are added on the half circle, respectively. The particle at x, the previous crack tip, is kept and split. All other particles associated with this point are removed in the next step. This is necessary since with such excessive refinement, very small particle masses and volumes would be obtained. A small value r also destroys the stable time step. The distance between the new (adaptively added) particles and the old particles is checked, too. If the distance undershoots a given value, the corresponding old particle is deleted. This ensures a larger stable time step.

For quasistatic behavior, r plays a secondary role. For dynamic behavior, r has to be chosen carefully, since the crack speed might be influenced. To obtain an appropriate crack speed, we divided the time step by a factor of three. Difficulties might occur for highly dynamic problems when a structure subjected to high loads such as in an explosion.

3.3 Implementation

In this subsection, the implementation of the discrete crack model will be described. With the introduction of the crack boundary and the particle split, it is possible to compute the relative displacement of the crack edges. The relative displacements are computed in a local coordinate system denoted by $\boldsymbol{\xi}$ and by a subscript l as shown in figure 11. The boundary particles are assigned to a coordinate system according to their corresponding crack segment. Since we use a total Lagrangian formulation (with a Lagrangian kernel), the coordinates of a point and the orientation of the coordinate system stay fixed once it is computed. It is not necessary to rotate the coordinate system as in some rotating crack models.

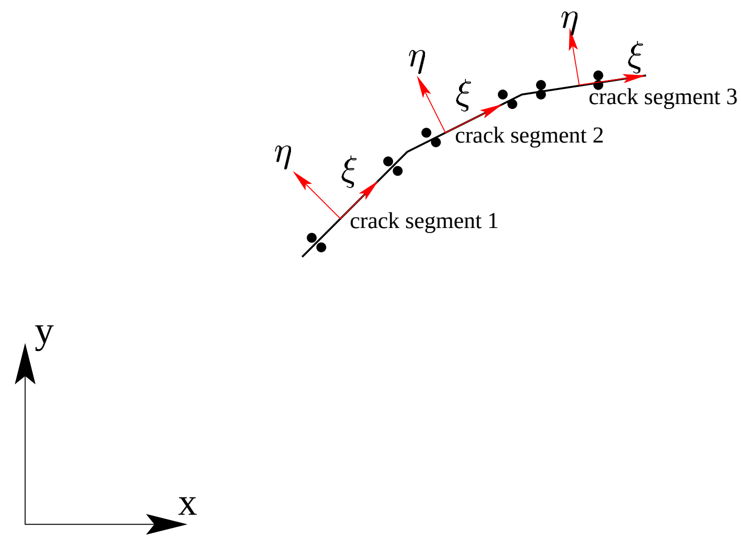

Figure 11: Relation between local crack coordinate system and global coordinate system

The relative displacements $\boldsymbol{\delta}_l = [w\ u]^T$, where w is the normal relative displacement of the crack edges, the crackwidth, and u is the tangential relative displacement according to the local coordinate system, are

$$\boldsymbol{\delta}_l = \mathbf{u}_l^A - \mathbf{u}_l^B \tag{30}$$

where the superscripts A and B indicate the 'left' and the 'right' hand side of the crack (see figure 1) and $\mathbf{u}_l$ is the displacement in the local coordinate system.

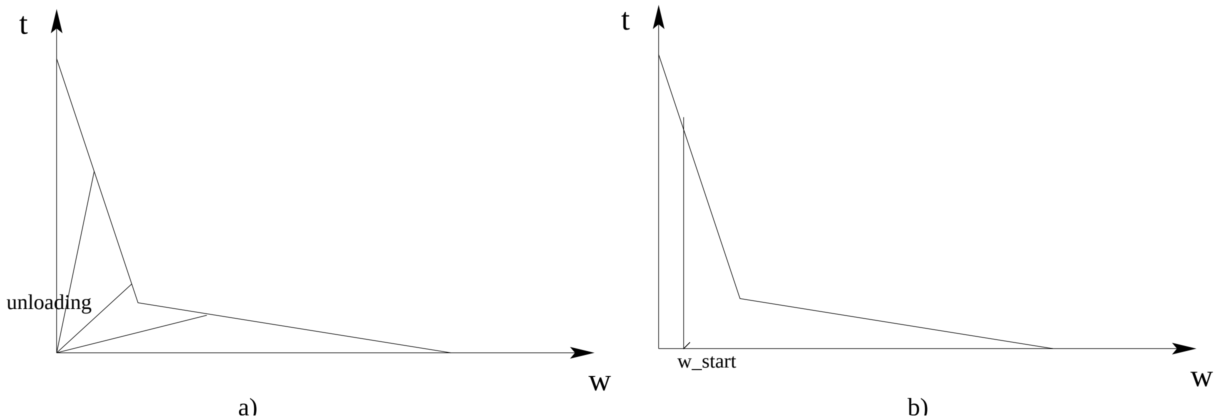

Figure 12: Discrete crack model

The traction crack opening model is expressed in terms of the relative displacements in a local coordinate system $\left(e_1^0, e_2^0\right)$ with e_1^0 tangent to the image of the crack in the undeformed configuration and e_2^0 normal to the image of the crack in the undeformed configuration. Therefore the displacements or relative displacements $\boldsymbol{\delta}_g = \mathbf{u}_g^A - \mathbf{u}_g^B$ in the global coordinate system have to be rotated in the local one. This can be done with the transformation matrix $\mathbf{T}$:

$$\mathrm{T} = \begin{bmatrix} cos\ \gamma & sin\ \gamma \\ -sin\ \gamma & cos\ \gamma \end{bmatrix}$$

The traction crack opening model can now be applied. The tractions in the local coordinate system have to be transformed by $\mathbf{T}$ into the global coordinate system where they are applied as external forces. In the unloading case, the traction will return to the origin of the traction crack opening curve as shown in figure 12a.

The transition from the tensile to the compressive regime and vice versa in a pure continuum mechanical description is handled easily as described in Rabczuk et al. [26]. Once a discrete crack with a crack boundary is introduced, we have to deal with contact if the crack closes. Consider the crack as illustrated in figure 13. The crack line is formed by the neighboring (crack boundary) particles of the corresponding crack side (left or right). We check if the crack boundary particle on the crack line of the opposite side penetrates the two corresponding crack lines (on the other side), e.g. contact for particle 3 is checked for segment 1 and 2 as illustrated in figure 13. If particle 3 penetrates e.g. segment 1, contact forces to the corresponding neighbor particles normal to the crack line are applied as shown on the RHS of figure 13, so that the penetrating particle stays on the appropriate side at the end of the time step. F_1, F_2 and F_3 in figure 13 denote the contact forces, d is the penetration depth and l_3 is the length of segment 1.

In our examples, no numerical instabilities were observed.

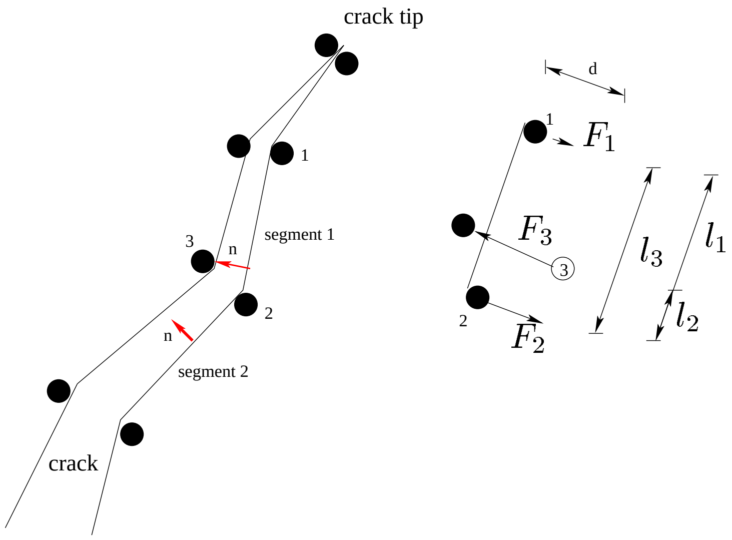

Figure 13: Imposing contact conditions on the crack boundary particles for a crack closing

4 Numerical results

4.1 The Arrea/Ingraffea beam

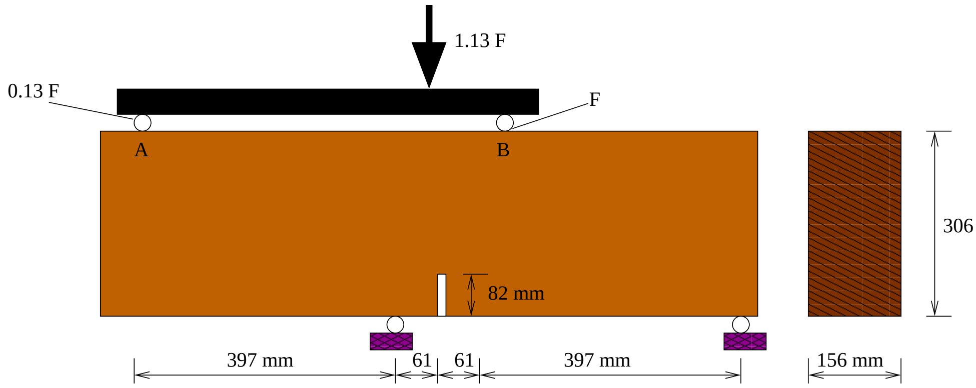

Figure 14: The tensile/shear beam from Arrea Ingraffea

The first example is the tensile/shear beam of Arrea and Ingraffea [2]. The notched beam is loaded at two points (A and B, see figure 14). The initial elastic modulus is 28,000 MPa. The beam fails due to a mixed tensile/shear failure. This problem is commonly used to test constitutive laws with respect to combined failure modes.

The load displacement (on the RHS of the notch) curve is shown in figure 15a. In addition

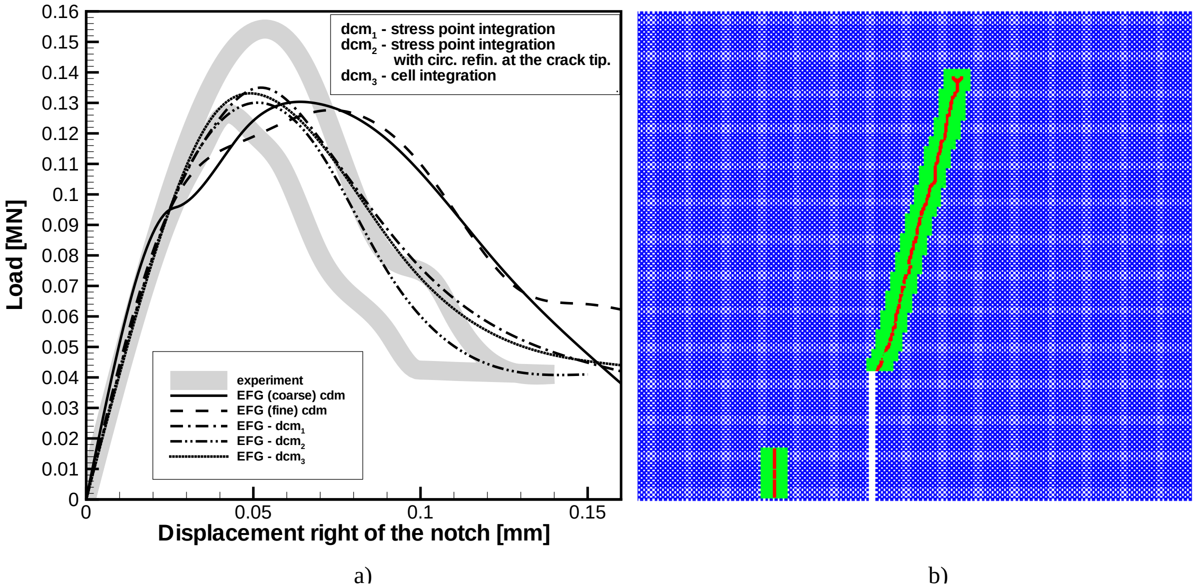

Figure 15: a) Load displacement curve, b) Crack pattern around the notch for the model dcm_2

to the results obtained with our discrete crack model (dcm), results with a complete continuum damage plasticity model (cdm) (see Rabczuk et al. [26]) and experimental data are given. Particularly the post peak behavior is modelled better by the discrete crack model than by the continuum damage model.

Three different approaches are used for the discrete crack model. Model dcm_1 uses the discrete crack model described in Section 3 where the integrals are evaluated by a nodal integration with stress points. No circular refinement around the crack tip is made. Model dcm_2 uses also a nodal integration and stress points for the computation of the integrals. An additional circular refinement around the crack tip is used where the radius of the circle is chosen to be $r = 0.95\ \delta x$, where δx is the minimum distance between particles. Additionally, the radius is decreased to $r = 0.5\ \delta x$. Since the load displacement curve differs minimally for the two different radii, the results for $r = 0.5\ \delta x$ are illustrated in figure 15a. For comparisons we have implemented a mixed discrete crack/smeared crack model dcm_3 as described in [16]. Model dcm_3 uses a background mesh for the integration. 25 Gauss points are used in the cells. It can be seen, that the discrete crack models agree pretty well in the experiment.

The crack pattern of the beam is illustrated in figure 16a for the full continuum model and in figures 16b and 16c for the discrete crack model dcm_1 and dcm_2, respectively. First, it can be seen, that with the discrete crack model, the crack resolution is much finer although fewer

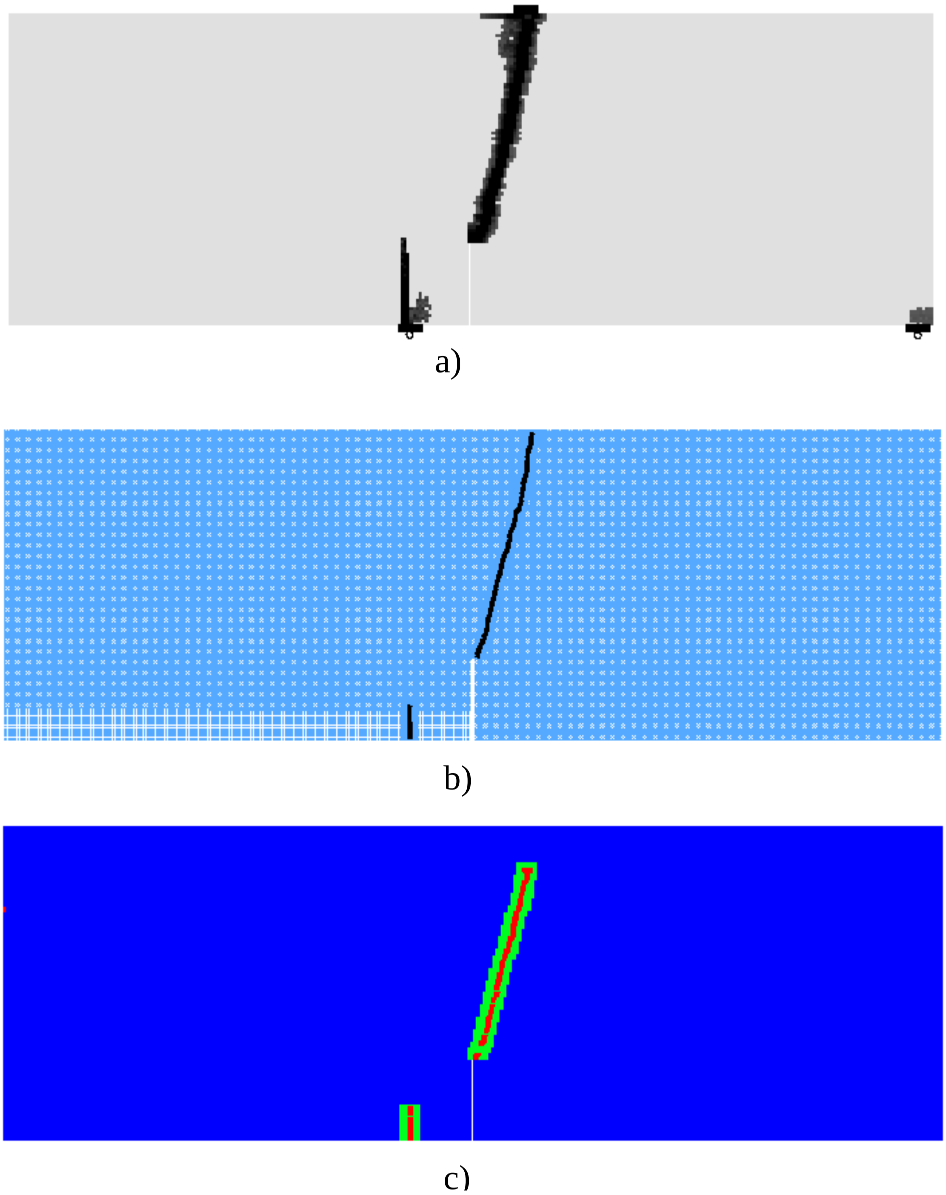

Figure 16: Crack pattern of the Arrea Ingraffea beam for a) a complete continuum model (see [25]), b) Model dcm_1, c) Model dcm_2

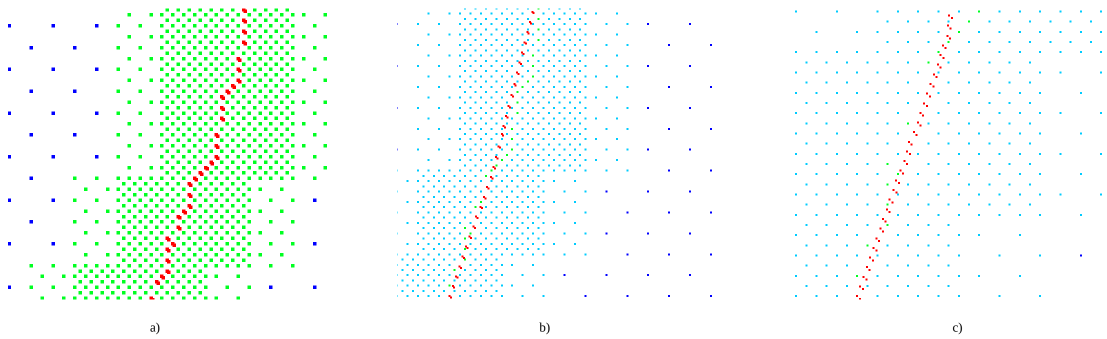

Figure 17: Crack pattern for a cutout of the beam for a) without circular refinement, b) with circular refinement for a refinement radius of $r = 0.95\ \delta x$, c) with circular refinement with $r = 0.5\ \delta x$

particles were needed with the adaptive refinement. While approximately 280,000 particles were used in the *cdm*-model, we started with 30,000 particles in our discrete crack models. The difference in the crack pattern between model dcm_1 and dcm_2 is small. However, for the dcm_1 model the number of particles increased by a factor of 2.5 while for the dcm_2 model the number of particles were increased by a factor of 1.8. Not only the higher number of particles but also the smaller particle separation in the dcm_2 model, which diminishes the time step, increases the computation time significantly. For this quasistatic problem, the differences between the two discrete crack models (dcm_1 and dcm_2) are not very obvious, but it will become so in dynamic problems.

With the discrete crack model, the crack widths can also be computed, which are comparable to experimental data. In figure 15b, the beam around the notch is illustrated for the dcm_2 model.

Cross sections for the different models are shown in figure 17. Figure 17a shows the crack for the dcm_1 model, in figure 17b, the results of the dcm_2 model with a refinement radius of $r = 0.95\delta x$ are illustrated. The red particles show the crack path. A zigzag pattern can be observed for the dcm_1 model . In the complete illustration, both computations give similar results (see figure 16b and 16c), but more particles were necessary to obtain the appropriate crack path when using no circular refinement. In figures 17b and 17c, the influence of the different radii ($r = 0.95\ min\ \delta x$ and $r = 0.5\ min\ \delta x$) for the circular refinement are illustrated. The influence of the size of the circle seems to be small in this application; this is true also for nearly straight crack paths and quasistatic loading conditions.

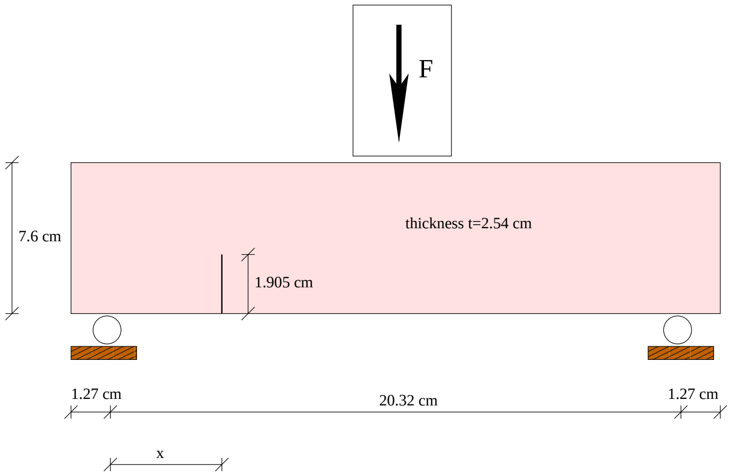

Figure 18: Test setup for the John and Shah beam

Table 1: Location of the notch

Number	Location x [cm]
1	2.38
2	2.85
3	3.02
4	5.08

4.2 John and Shah beam

John and Shah [20] performed a series of static and dynamic experiments on notched concrete beams. Figure 18 shows the test set up. Table 1 lists the different locations of the notch. They varied the load rate and the location of the notch. The rate of loading ranged from a slow strain rate of $10^{-6}/s$ for the quasistatic experiments to a dynamic load with strain rates of $0.5/s$. Two different failure modes were observed in the experiments as illustrated in figure 19. The first one is a pure mode I failure in the middle of the beam, the second one is a mixed mode failure where the crack started to propagate from the notch. The transition from the mode I to mixed mode failure depends on the location of the notch and differs for the dynamic and the static loading conditions (see figure 19). For the same location of the notch, the slope of the crack (for the mixed mode failure) for the quasistatic and dynamic loading is almost equal. We study here both dynamic and quasistatic loading. The load is applied via a boundary velocity condition given by John and Shah [20].

First, we focus on the notched beam number 4 ($x = 5.08\ cm$, see table 1) under dynamic loading. EFG with stress point integration is applied. Two simulations were performed, one

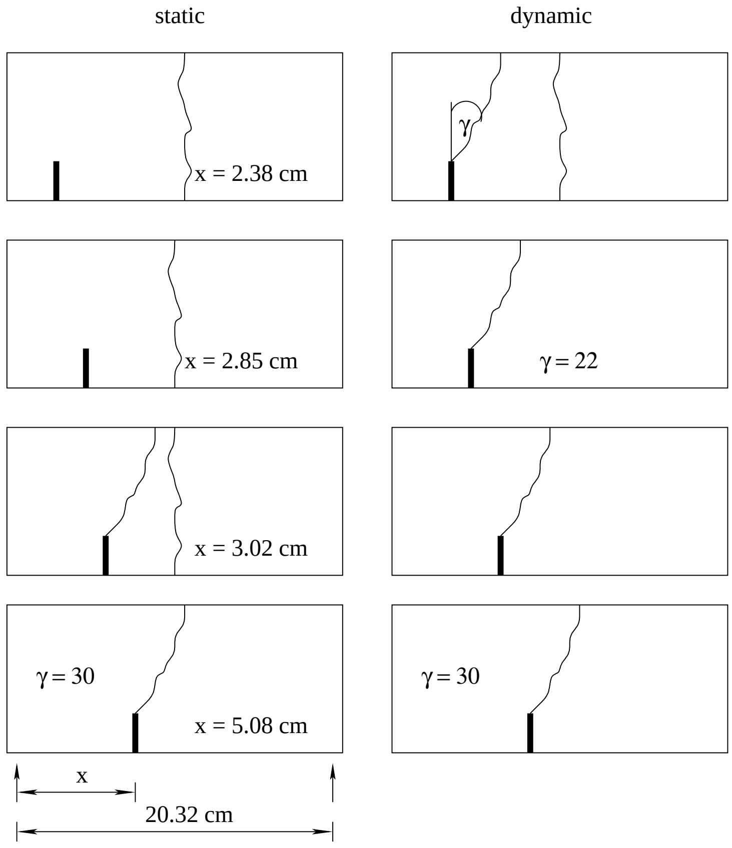

Figure 19: Crack patterns of the John and Shah [20] beam for different locations of the notch for quasistatic and impact loading

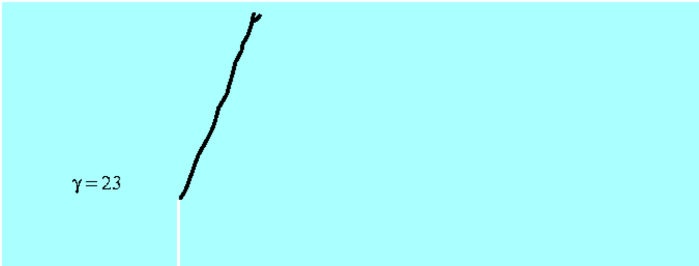

a)

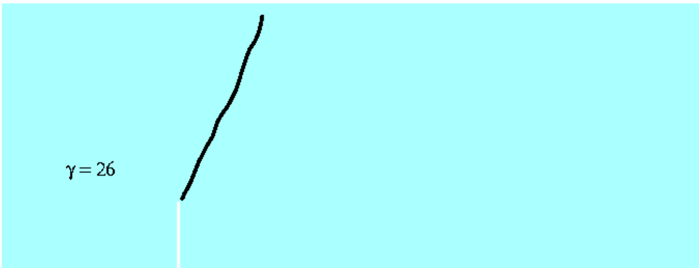

b)

Figure 20: Crack pattern of the John and Shah beam under impact loading for a location of the notch: x=5.08cm, a) for the dcm_2 model (with circular refinement), b) for the dcm_1 model (without circular refinement)

with circular refinement (model dcm_2, see figure 20a) and one without (model dcm_1, see figure 20b). The radius for the circular refinement was $r = 0.5 \; min \; \delta x$. The crack has an angle of 23^o against the y-axis for the first computation (see figure 20a), which matches the experimental data pretty well, see figure 19. Without the circular refinement, an angle of 26^o with the global y-axis is obtained, but the number of particles was two times higher than in the computation with circular refinement. At this point it should be mentioned that the experiments also exhibit some scatter. The crack path for the quasistatic computation with the circular refinement is similar to that in the dynamic loading. In figure 21 the crack path from the numerical computation is compared to the corresponding experiment. The agreement is very good.

Finally, we tried to reproduce the transition point of the beam failure modes as illustrated in figure 19. For the quasistatic loading, the transition point was computed quite well for a notch with a distance of 3 cm to the support, see figure 22a. In the experiments this transition point was observed for a notch with $x = 3.02cm$. In the dynamic loading the transition took place for $x = 2.29cm$ which is 10% closer to the support than observed in the experiments, see figure 19 and 22b. This maybe due to neglecting time-dependent effects in our discrete crack traction law. It can be seen that the the slope of the crack path from the notch gets steeper with decreasing distance of the notch to the support.

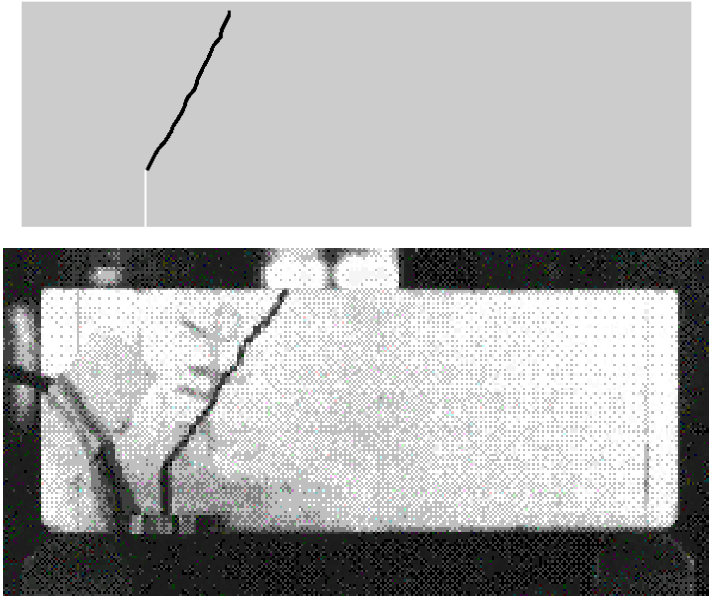

Figure 21: Comparison of the computed and observed crack pattern of the John and Shah beam under quasistatic loading

5 Conclusion

A meshfree method that allows a transition from continuum to discrete cracks with arbitrary paths and adaptivity has been described. The discrete crack is treated as an internal boundary. The model is integrated in a meshfree particle code since meshfree particle methods are well suited for arbitrary crack propagation problems. It is easy possible to introduce boundaries and add particles adaptively. The particles were added in a rectangular pattern. Since a zigzag pattern was observed in the computation with only rectangular refinement, additional particles were added in a half circle around the crack tip; these were deleted after the crack advanced. The choice of the refinement radius r of this half circle was studied. With increasing r, an increasing crack speed was observed. Decreasing the stable time step with a factor of three was able to overcome this dependency. However, the choice of a constant r is a critical point in the computation.

The model is applied to concrete materials and mixed mode fracture problems, the Arrea and Ingraffea beam and the John and Shah beam. We were able to reproduce the crack patterns and their dependence on the notch and the load displacement curves quite well. Some discrepancies occur when the beam is loaded dynamically. One reason may be that rate effects in the traction crack opening model are not considered. These may play a significant role under high loading velocities as shown by Eibl et al. [14, 15].

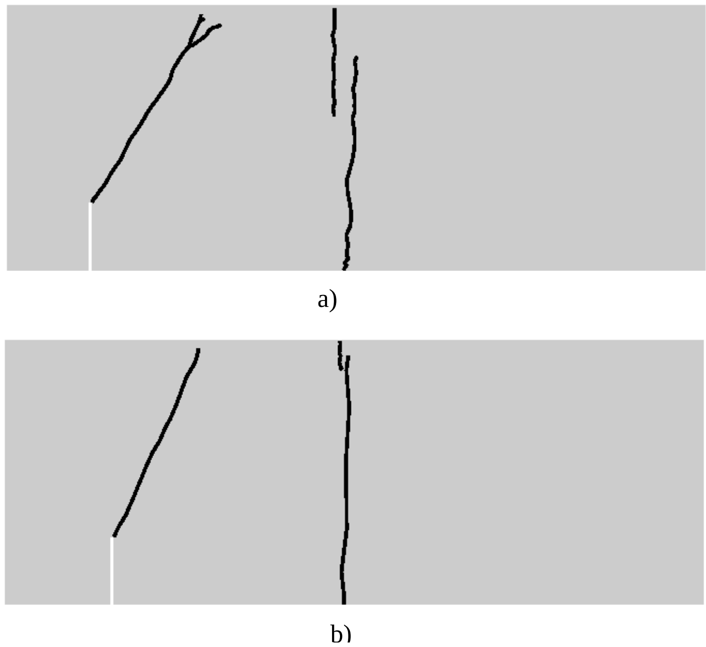

Figure 22: Computed crack pattern of the John and Shah beam near the transition in the failure mode, a) under quasistatic loading, b) under dynamic loading

Acknowledgments: The support of the Army Research Office and the Office of Naval Research are gratefully acknowledged.

References

[1] Eurocode 2: Planung von Stahlbeton- und Spannbetontragwerken. Teil 1: Grundlagen und Anwendungsregeln fuer den Hochbau, in Betonkalender 1993, T. II, Ernst und Sohn, Berlin, 1993.

[2] M. Arrea and A.R. Ingraffea. Mixed-mode crack propagation in mortar and concrete. Technical report, No. 81-13, Dept. of Struct. Eng., Cornell University Ithaka, N.Y., 1982.

[3] J.H. Prevorst B. Loret. Dynamic strain localization in elasto-(visco)-plastic solids, part1: General formulation and one-dimensional examples. Computer Methodes in Applied Mechanics and Engineering, 83:247–273, 1990.

[4] S. Bazant and T. Belytschko. Wave propagation in a strain-softening bar: Exact solution. Journal of Engineering Mechanics-ASCE, 111(3):381–389, 1985.

[5] T. Belytschko, H. Chen, J. Xu, and G. Zi. Dynamic Crack Propagation Based on Loss of Hyperbolicity and A New Discontinuous Enrichment.

[6] T. Belytschko, M. Fleming, D. Organ, Y. Krongauz, and P. Krysl. Meshless methods: An overview and recent developments. Comp. Meth. Appl. Mech. Engn, 139:3–48, 1996.

[7] T. Belytschko, Y. Guo, W.K. Liu, and S.P. Xiao. A unified stability analysis of meshless particle methods. Int. J. Numer. Meth. Engng, 48:1359–1400, 2000.

[8] T. Belytschko, W.K. Liu, and B. Moran. Nonlinear Finite Elements for Continua and Structures. John Wiley and Sons, LTD, New York, 2000.

[9] T. Belytschko and Y.Y. Lu. Element-free galerkin methods for static and dynamic fracture. Int. J. Solids Strucutres, 32:2547–2570, 1995.

[10] T. Belytschko, Y.Y. Lu, and L. Gu. Element-free galerkin methods. International Journal for Numerical Methods in Engineering, 37:229–256, 1994.

[11] T. Belytschko and I.S. Yeh. The splitting pinball algorithm for contact-impact problems, computer methods in applied mechanics and engineering. 105:375–393, 1993.

[12] T. Belytschko, H.J. Yen, and R. Mullen. Mixed methods for time integration. Computer Methods in Applied Mechanics and Engineering, 17:259–275, 1979.

[13] H. Chen. Enriched finite element methods and its applications. PhD-thesis, Northwestern University, Department of Mechanical Engineering, Computational Mechanics Group,, Dezember 2002.

[14] J. Eibl. Ein neuer Ansatz fuer ein Stoffgesetz zur Beruecksichtigung grosser Dehngeschwindigkeiten bei zugbeanspruchtem Beton. Waubke Festschrift, BMI, Schriftenreihe des Instituts fuer Baustoflehre und Materialpruefung der Universitaet Innsbruck, 9/96, 1996.

[15] J. Eibl and M. Curbach. An attempt to explain strength increase due to high loading rates. Nuclear Engineering and Design, 112:45–50, 1989.

[16] Haeusler-Combe. Elementfreie Galerkin-Verfahren, Grundlagen und Einsatzmoeglichkeiten. Habilitation, Institut fuer Massivbau und Baustofftechnologie, Universitaet Karlsruhe, 2001.

[17] S. Hao, W.K. Liu, and T. Belytschko. Modeling and simulation of damage induced crack using meshfree methods. In Proceedings of the WCCM IV, Argentina, 1998.

[18] H.K. Hilfsdorf and H.W. Reinhardt. Beton. Betonkalender 97, Teil 1, Verlag Ernst u. Sohn, Berlin, 1997.

[19] T.J.R. Hughes and W.K. Liu. Implicit-explicit finite elements in transient analysis: implementation and numerical examples. Journal of Applied Mechanics, 45:375–378, 1978.

[20] J.R. John and S.P. Shah. Mixed mode fracture of concrete subjected to impact loading. ASCE J. Struc. Eng., 116:582–602, 1990.

[21] S. Mindess. Fracture Prosess Zone Detection. Fracture Mechanics Test Methods for Concrete, RILEM Report 89-FMT, Chapman and Hall, London, 1991.

[22] A. Needleman. Material rate dependence and mesh sensivity on localization problems. Computer Methodes in Applied Mechanics and Engineering, 67:69–86, 1988.

[23] D. Organ, M. Fleming, T. Terry, and T. Belytschko. Continuous meshless approximations for nonconvex bodies by diffraction and transparency. Comp. Mech., 18:225–235, 1996.

[24] T. Rabczuk and T. Belytschko. Adaptivity in explicit meshfree particle methods. submitted.

[25] T. Rabczuk, T. Belytschko, and S.P. Xiao. Stable particle methods based on lagrangian kernels. submitted to Computer Methods in Applied Mechanics and Engineering.

[26] T. Rabczuk and J. Eibl. Simulation of high velocity concrete fragmentation using sph/mlsph. Int. J. Numer. Meth. Engng, 56:1421–1444, 2003.

[27] Schmidt-Hurtienne. Ein dreiaxiales Schaedigungsmodell zur Beschreibung des Dehnrateneffektes von Beton. Dissertation, Institut fuer Massivbau und Baustofftechnologie, Universitaet Karlsruhe, 2000.